Angewandte Chemie
Eine Zeitschrift der Gesellschaft Deutscher Chemiker

Supporting Information

# Strong Valence Band Convergence to Enhance Thermoelectric Performance in PbSe with Two Chemically Independent Controls

*Zhong-Zhen Luo, Songting Cai, Shiqiang Hao, Trevor P. Bailey, Ioannis Spanopoulos, Yubo Luo, Jianwei Xu, Ctirad Uher, Christopher Wolverton, Vinayak P. Dravid, Qingyu Yan,* and Mercouri G. Kanatzidis**

ange_202011765_sm_miscellaneous_information.pdf

# SUPPORTING INFORMATION

## Experimental Procedures

**Synthesis.** The nominal compositions of $Pb_{0.99}Ag_{0.01}Se$-x%SrSe (x = 0, 1, 1.5, 2, 3, and 4) and $Pb_{0.99}Ag_{0.01}Se$-y%BaSe (y = 1, 2, 3, 4 and 5) were synthesized by mixing the high purity starting materials (Pb wire, 99.99%, American Elements, USA; Se shot, 99.999%, Alfa Aesar, USA; Sr chunk, 99.9%, Sigma-Aldrich, USA; Ba rod, 99.9%, Sigma Aldrich, USA; and Ag shots, 99.99%, Sigma-Aldrich, USA) in 13 mm diameter carbon coating quartz tubes under $N_2$-filled glove box. The surfaces of Pb wire and Ba rod were scraped off prior to use for removing any oxide contamination. PbSe-x%SrSe (x = 0, 1, 1.5, 2, 3, and 4) and PbSe-y%BaSe (y = 1, 2, 3, 4 and 5) were also synthesized in order to measure the band gap. The tubes were flame-sealed at a residual pressure of ~$2 \times 10^{-3}$ torr, then slowly heated to 1473 K over 12 h in a box furnace, soaked at this temperature for 6 h, followed by furnace cooling to room temperature. For a typical experiment, the following amounts were used: Pb (10 g, 48.26 mmol), Se (3.9085 g, 49.50 mmol), Ag (0.0534 g, 0.50 mmol), and Sr (0.0651 g, 0.74 mmol) to prepare a ~14 g ingot of $Pb_{0.99}Ag_{0.01}Se$-1.5%SrSe.

**Densification.** The cast ingots were hand ground into a fine powder using agate mortar and pestle. The powder was put inside a 12.7 mm diameter graphite die and subsequently sintered by using the Spark Plasma Sintering (SPS) technique (SPS-211LX, Fuji Electronic Industrial Co. Ltd.) at 923 K for 5 min under an axial compressive stress of 40 MPa in vacuum. Highly dense disk-shaped pellets (> 96.5% theoretical density) with a thickness of ~10 mm were obtained.

**Powder X-ray Diffraction (PXRD) Characterization.** The finely ground powder samples were used for PXRD using a Rigaku Miniflex powder X-ray diffractometer with Ni-filtered Cu $K_\alpha$ ($\lambda$ = 1.5418 Å) radiation operating at 40 kV and 15 mA and with a $K_\beta$ filter.

**Band Gap Measurement.** The room temperature optical diffuse reflectance spectra for PbSe-x%SrSe and PbSe-y%BaSe samples were recorded in the wave number range 4000 − 400 $cm^{-1}$ using a Nicolet 6700 FT-IR spectrometer. The generated reflectance data was transformed to absorbance by using the Kubelka-Munk formula: $\alpha/S' = (1 - R)^2/(2R)$, where $R$, $\alpha$ and $S'$ represent the reflectance, absorption, and scattering coefficients, respectively.[1]

**Photoemission Spectroscopy.** The work functions (valence band maxima) were measured by photoemission yield spectroscopy in air (PYSA, AC-2, Riken-Keiki).[2] In PYSA, the sample is scanned by tunable monochromatic ultraviolet light (UV, 4.2–6.2 eV) under ambient conditions, and the number of generated photoelectrons is measured at each excitation energy. Photoelectrons are only generated when the photon energy is higher than the work function. The work function is determined by fitting the linear region of the PYSA spectra.

**Electrical Transport Properties.** The $\sigma$ and $S$ of SPSed samples were simultaneously measured using an Ulvac Riko ZEM-3 instrument under a low-pressure Helium atmosphere from room temperature to 923 K. For the test, the obtained SPSed pellets were cut and polished into bars with a size of about 11 mm × 4 mm × 4 mm. The uncertainty of the electrical conductivity and Seebeck coefficient is about 5% for this measurement, respectively.[3]

**Thermal Conductivity.** The total thermal conductivity ($\kappa_{tot}$) was estimated using the relationship: $\kappa_{tot} = D \cdot C_p \cdot \rho$, where $D$, $C_p$, and $\rho$ are the thermal diffusivity, specific heat capacity, and density, respectively. The $D$ was measured on a Netzsch LFA457 under a continuous $N_2$ flow from 300 to 923 K. The polished samples with approximate dimensions of 6 mm × 6 mm × 2 mm were coated with a thin layer of graphite to minimize errors from the emissivity of samples during the measurement. The results of $D$ were analyzed using a Cowan model with pulse correction. The $C_p$ was calculated using the equation $C_p$ (per unit mass) = $0.170778 + 2.648764 \times 10^{-5} \times T$(/K) J $g^{-1}K^{-1}$.[4] [5] The $\rho$ was obtained by calculating the mass and dimensions of the sample. Considering all the uncertainties from $D$ (~5%), $C_p$ (~15%) and $\rho$ (~5%), the combined uncertainty for all measurements involved for the evaluation of $ZT$ was ~20%.

**Transmission Electron Microscopy (TEM).** TEM analyses were done with an JEOL ARM 300 microscope operated at 300 kV. The electron-beam transmitted TEM specimens were prepared by hand grinding and polishing, followed with Ar-ion milling (3 kV for ~1 hour until a hole is formed, followed by ion cleaning with 0.3 kV for 1 hour) under low temperature (liquid nitrogen stage).

**Density Functional Theory (DFT) Calculations**. We use DFT calculations to relax geometries of the crystal structures. The DFT total energy calculations are completed within the generalized gradient approximation (GGA). The Perdew-Burke-Ernzerhof exchange correlation functional with Projector Augmented Wave potentials are applied.[6] We used plane wave basis sets with an energy cutoff of 500 eV and periodic boundary conditions for solids as implemented in the Vienna ab initio simulation package.[7] We set the total energy convergence within 3 meV/cation with a very dense k-meshes corresponding to 4000 k-points per reciprocal atom in the Brillouin zone. For the electronic band structure at elevated temperature, we simply use an atomic structure with expanded lattice constants to

mimic temperature effects. The atom-projected densities of states are the projections of particular orbitals on the wave function, corresponding to the number of electron states per unit volume per unit energy. On the basis of the band structure of the rock-salt phase, the effective masses are calculated by fitting the actual E−k diagram around the valence band maximum and conduction band minimum. For different directions, the effective mass $m^*$ is defined as $m^* = \hbar\left(\frac{\partial^2 E}{\partial k^2}\right)^{-1}$.

**Hall Measurements.** The Hall effect was measured at room temperature and up to ~800 K for select samples. An AC 4-probe method in a homemade system was implemented with excitation fields of ± 0.5 Tesla to negate any probe misalignment. The homemade system uses an air-bore, helium-cooled superconducting magnet to generate the field within a high temperature oven that surrounds the Ar-filled sample probe. Specimens were cut to sizes of ~1 mm × 3 mm × 8 mm, polished with 2000 grit SiC paper and secured within the probe by pressure contacts. The estimated error for the Hall coefficient, $R_H$, is based on the standard deviation of several data points at a single temperature, and is approximately 5%. The carrier concentration is extracted from the Hall coefficient assuming a single carrier, *i.e.* $n = 1/(e|R_H|)$, where $e$ is the electron charge. The error in the carrier concentration is derived from the error in the Hall coefficient. The Hall mobility ($\mu_H$) was determined as $\mu_H = \sigma R_H$, with $\sigma$ the electrical conductivity at the same temperature as $R_H$.

## Results and Discussion

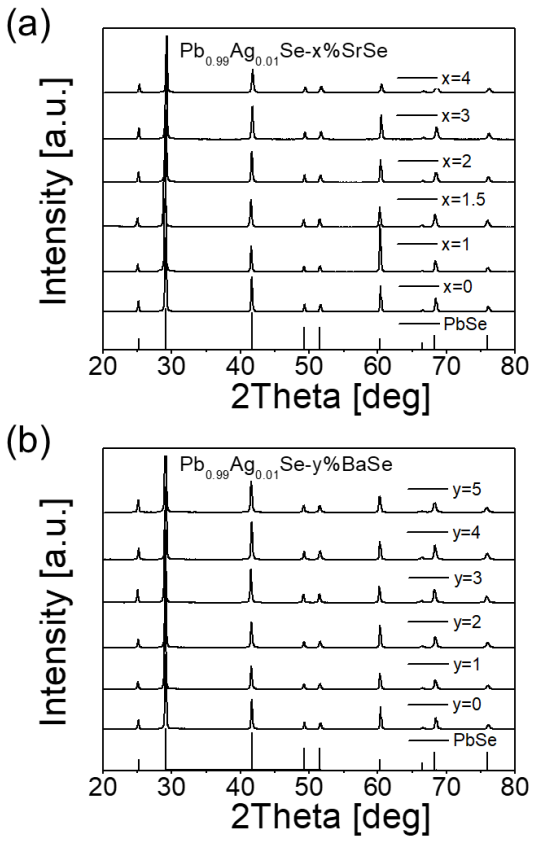


**Figure S1.** PXRD patterns of $Pb_{0.99}Ag_{0.01}Se$-x%SrSe (a) and $Pb_{0.99}Ag_{0.01}Se$-y%BaSe (b) samples with varied doping levels, with all peaks indexed by the PbSe cubic phase (JCPDS #06-0354).

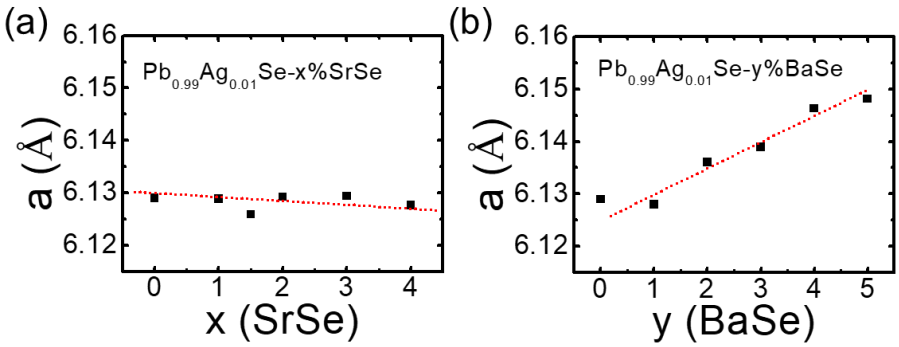


**Figure S2.** Refined lattice parameters of $Pb_{0.99}Ag_{0.01}Se$-x%SrSe (a) and $Pb_{0.99}Ag_{0.01}Se$-y%BaSe (b) samples with varied doping levels, indicating a contraction and expansion of the lattice for SrSe and BaSe alloying, respectively. The dashed line is a guide to the eye. The refined lattice parameters of $Pb_{0.99}Ag_{0.01}Se$-x%SrSe slightly decrease with increasing SrSe fraction because of the smaller atomic radius of $Sr^{2+}$ (~1.13 Å) compared to $Pb^{2+}$ (~1.20 Å), indicating the solubility of SrSe in PbSe.[8] On the contrary, the lattice parameters for BaSe-alloyed samples noticeably increase due to the larger atomic radius of $Ba^{2+}$ (~1.35 Å). These results confirm the substitution of $Pb^{2+}$ with $Sr^{2+}$ or $Ba^{2+}$ in the PbSe lattice.

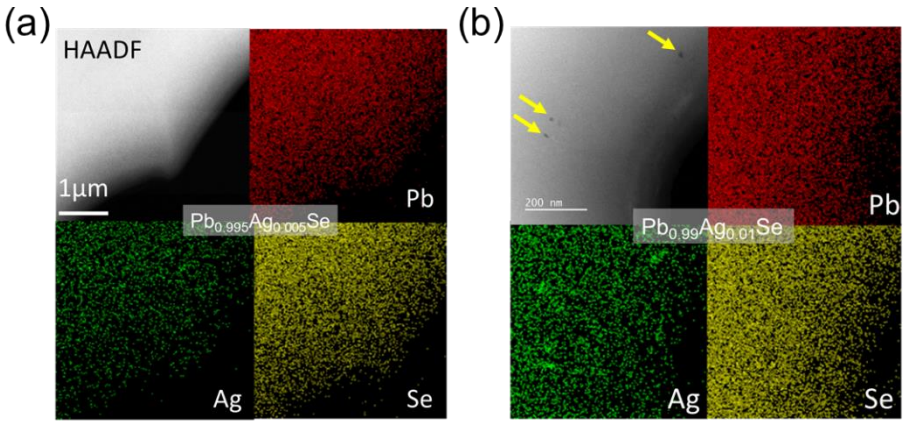


**Figure S3**. HAADF image and the corresponding EDS mappings of $Pb_{0.995}Ag_{0.005}Se$ (a) and $Pb_{0.99}Ag_{0.01}Se$ (b).

**Electronic Energy Band Gap and Photoemission Yield Spectroscopy in Air (PYSA).** The electronic energy band gap is systematically enlarged with increasing SrSe or BaSe fractions (Figures S4a and S4b). In detail, for SrSe-alloyed samples, the band gap expands slightly from ~0.23 eV for pure PbSe to ~0.28 eV for the x = 4 sample. For BaSe-alloyed samples, the band gap increases significantly from ~0.23 eV to ~0.44 eV for the y = 5 sample. These results are consistent with the very wide band gaps of SrSe ($E_g \approx$ 3.7 eV)[9] and BaSe ($E_g \approx$ 3.6 eV),[10] and previous reports.[11] As we will see below, the enlarged band gap is helpful in the suppression of bipolar electronic and thermal conductivity at high temperatures.

The work functions of undoped PbSe-x%SrSe and PbSe-y%BaSe were probed by PYSA at room temperature using the PYSA technique.[2a, 12] Because of the degenerately doped nature of the samples, the work functions are equivalent to the energies of the valence band maximum (VBM, L point) versus vacuum. The conduction band minimum (CBM) was estimated by adding the experimentally measured band gap to the energy of the VBM. The values of the VBM and CBM energies are displayed in Figures S4c and S4d for the PbSe-x%SrSe and PbSe-y%BaSe samples, respectively. The PYSA results show that the VBM moves deeper in energy from ~4.93 eV for pure PbSe to ~5 eV for both the SrSe- and BaSe-alloyed samples. On the other hand, the CBM remains approximately unchanged for SrSe-alloyed samples, but for the BaSe-alloyed y = 5 sample moves significantly higher in energy from ~4.7 eV in pure PbSe to ~4.56 eV.

These PYSA-derived energy data can help us estimate the energy offset, $\Delta E_v$, between the light valence band (*L* point) and the heavy valence band (along $\Sigma$) in our samples. For pristine PbSe the energy offset is ~0.25 eV at room temperature[12-13] and places the energy of the heavy valence band maximum (along $\Sigma$) at ~5.18 eV. Furthermore, by assuming the heavy valence band maintains a constant energy with respect to the vacuum, which is supported by our DFT calculations, $\Delta E_v$ can be calculated from the measured work functions. The values are plotted in Figures S4e and S4f for PbSe-x%SrSe and PbSe-y%BaSe samples, and they indicate that $\Delta E_v$ is reduced from ~0.25 for pure PbSe to ~0.18 eV for both SrSe- and BaSe-alloyed samples at room temperature. This value is very

close to the $\Delta E_v$ of PbTe itself. It has positive implications in improving the p-type transport in PbSe from a single band to a two band transport motif and achieving an enhancement in the overall figure of merit.

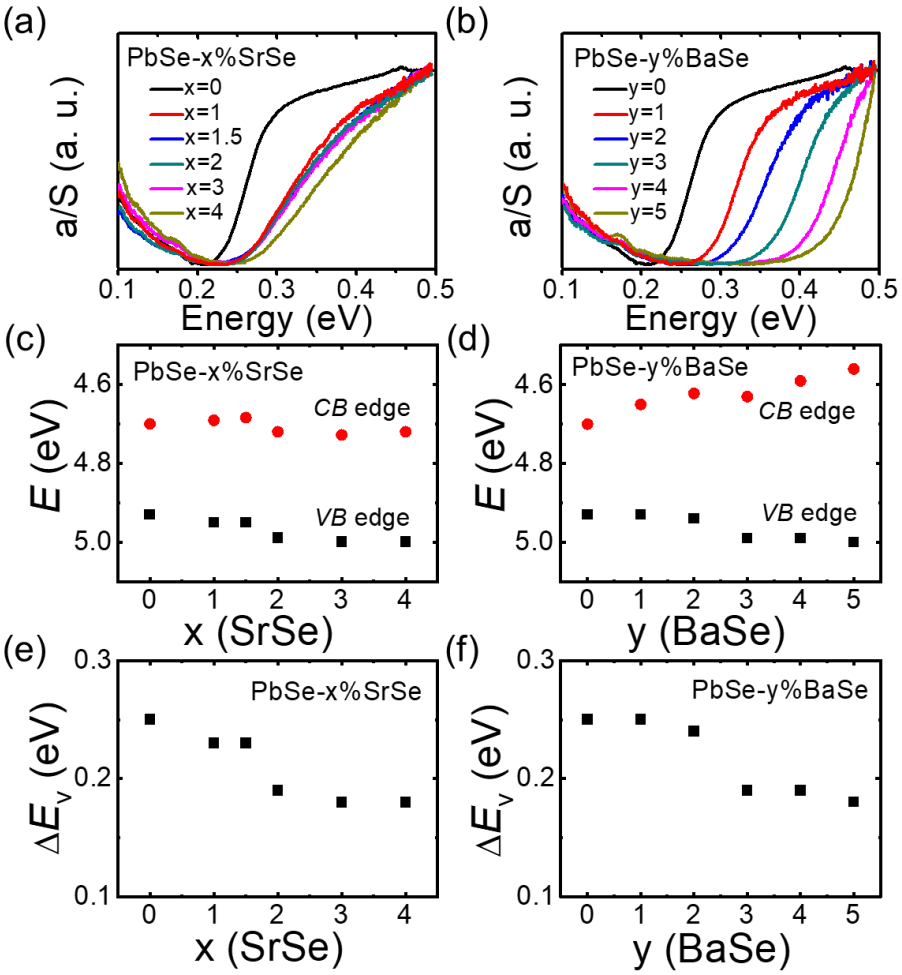


**Figure S4.** Infrared absorption spectra for $Pb_{0.99}Ag_{0.01}Se$-x%SrSe (a) and $Pb_{0.99}Ag_{0.01}Se$-y%BaSe (b) samples. Energies of the valence band maximum (VBM) and conduction band minimum (CBM) for PbSe-x%SrSe (c) and PbSe-y%BaSe (d) samples extracted from the linear regions of the photoemission spectra; and experimentally estimated energy differences between the L- and Σ-valence bands for PbSe-x%SrSe (e) and PbSe-y%BaSe (f) samples.

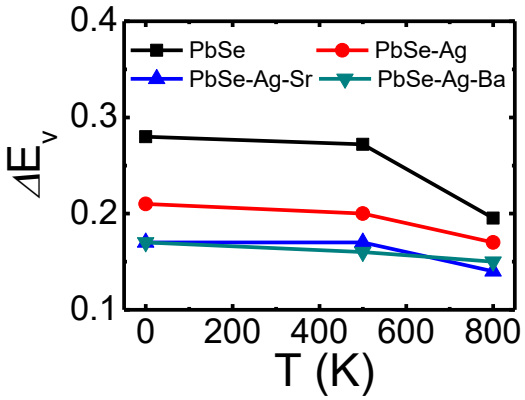


**Figure S5.** Temperature-dependent $\Delta E_v$ for Ag-doped PbSe, Ag-doped and SrSe alloyed PbSe, and Ag-doped and BaSe alloyed PbSe with pure PbSe for comparison.

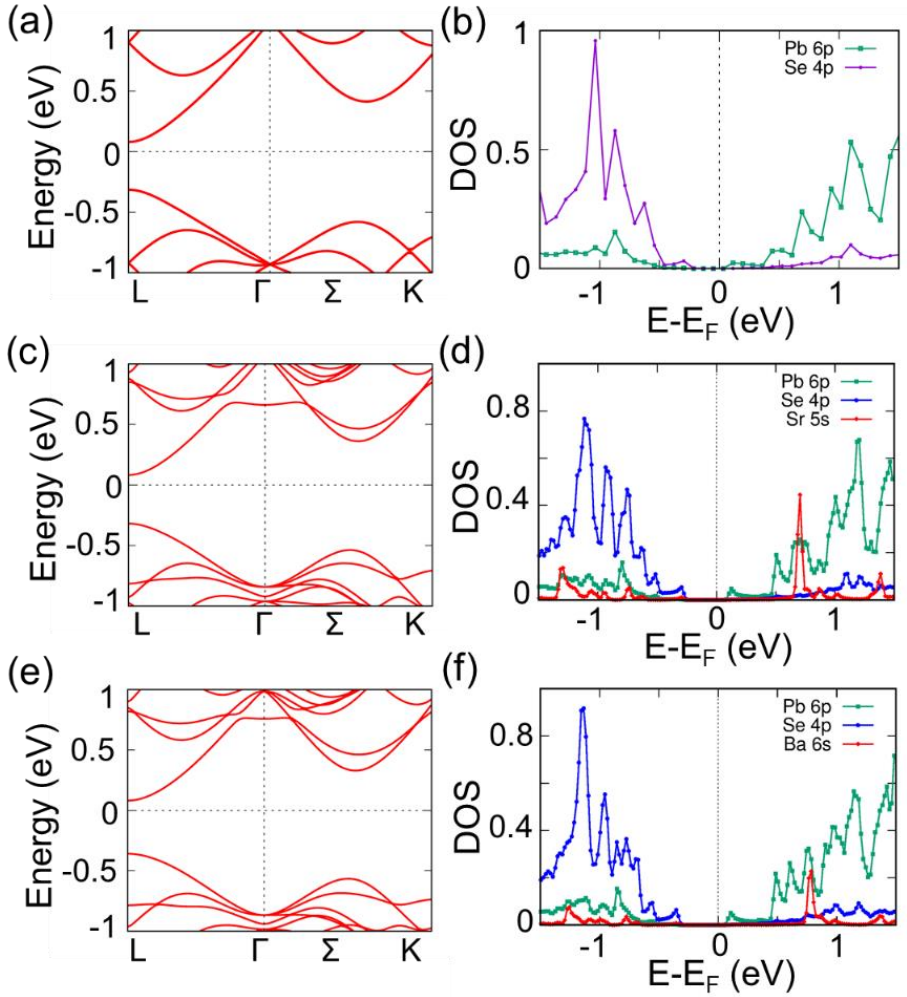


**Figure S6.** Band structure of pure PbSe with $\Delta E_v$ ~0.28 eV (a); SrSe-alloyed PbSe with $\Delta E_v$ ~0.21 eV (c); BaSe-alloyed PbSe with $\Delta E_v$ ~0.20 eV (e); and corresponding density of states with only one atom in each species for pure PbSe (b); SrSe-alloyed PbSe (d); and BaSe-alloyed PbSe (f) at 0 K, where the corresponding states with only one atom in each species are displayed to clearly show their contribution.

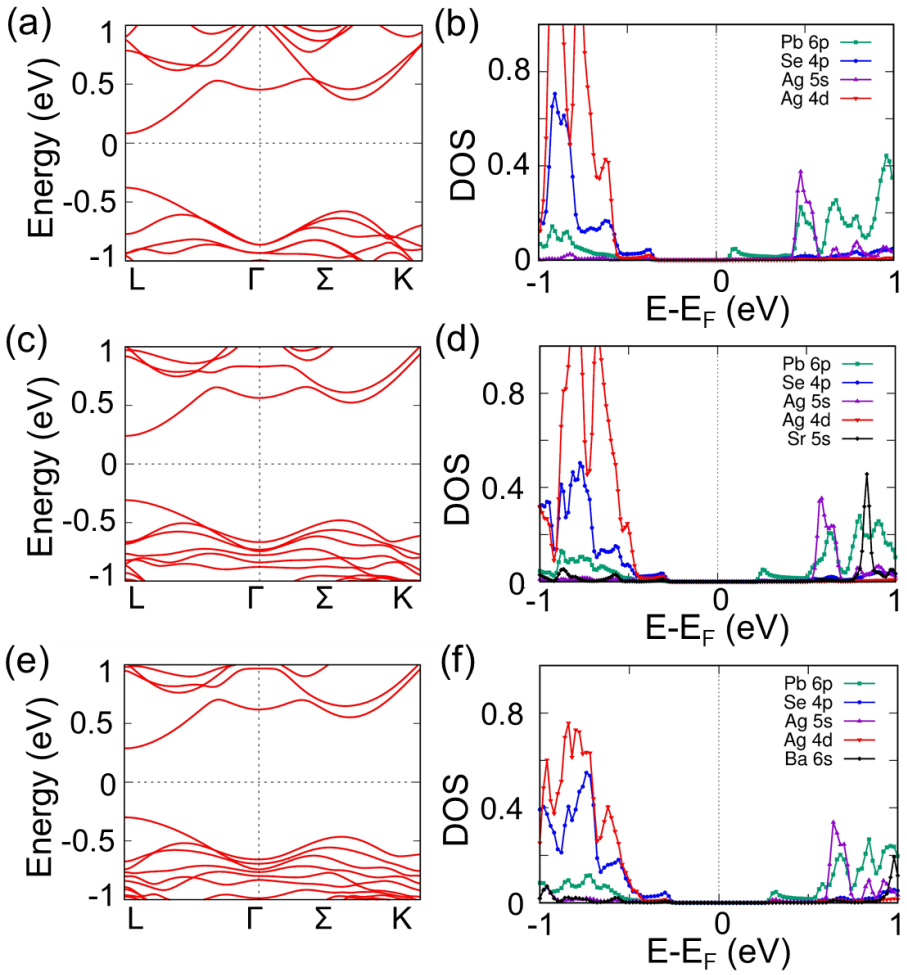


**Figure S7**. Band structure of Ag-doped PbSe with $\Delta E_v$ ~0.20 eV (a); Ag-doped and SrSe alloyed PbSe with $\Delta E_v$ ~0.17 eV (c); Ag-doped and BaSe alloyed PbSe with $\Delta E_v$ ~0.16 eV (e); and corresponding density of states with only one atom in each species for Ag-doped PbSe (b); Ag-doped and SrSe alloyed PbSe (d); and Ag-doped and BaSe alloyed PbSe (f) at 500 K, where the corresponding states with only one atom in each species are displayed to clearly show their contribution.

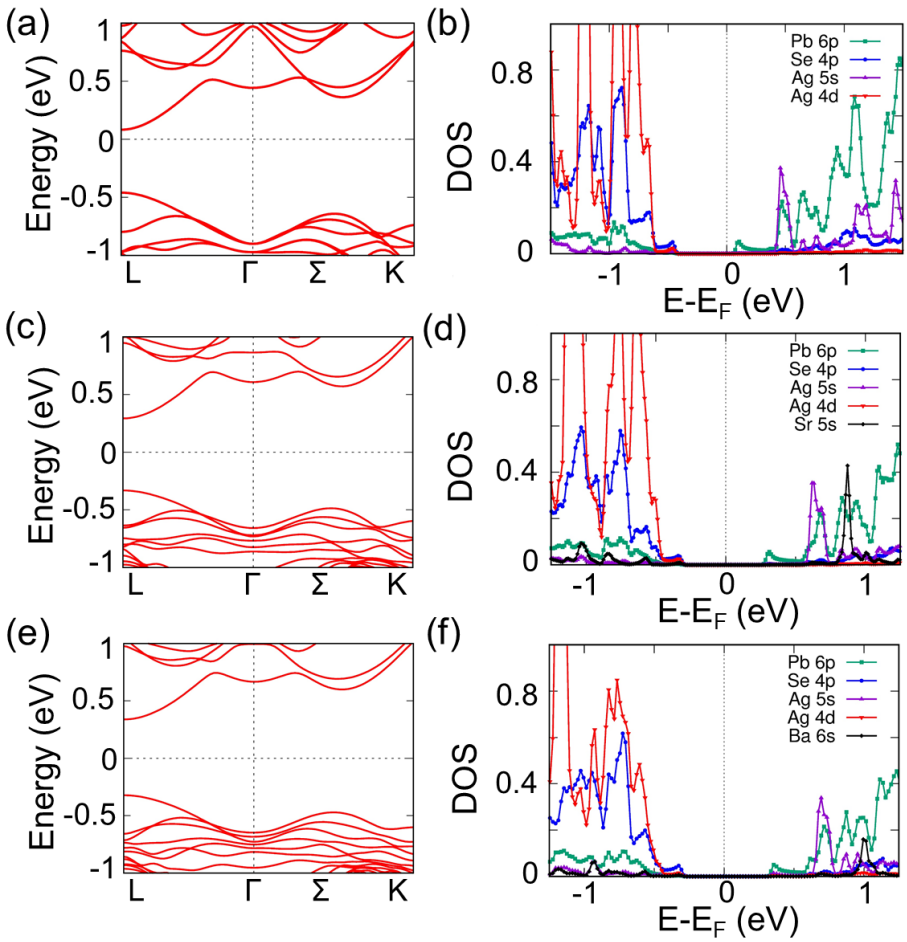


**Figure S8**. Band structure of Ag-doped PbSe with $\Delta E_v$ ~0.17 eV (a); Ag-doped and SrSe alloyed PbSe with $\Delta E_v$ ~0.14 eV (c); Ag-doped and BaSe alloyed PbSe with $\Delta E_v$ ~0.15 eV (e); and corresponding density of states with only one atom in each species for Ag-doped PbSe (b); Ag-doped and SrSe alloyed PbSe (d); and Ag-doped and BaSe alloyed PbSe (f) at 800 K, where the corresponding states with only one atom in each species are displayed to clearly show their contribution.

# SUPPORTING INFORMATION

**Discordant nature of Ag in PbSe**. It is critical to examine the local environment of doped Ag atoms since the occupy octahedral sites in PbSe. It is well known that silver atoms strongly favor tetrahedral,[14] trigonal planar[15] or linear sites[16] in crystalline solids and molecules. The imposed occupation of octahedral sites as is the case in PbSe is generally unfavorable and the non-isovalent $Ag^{+}$ atom has the tendency to move away from the center in order to achieve something resembling tetrahedral, trigonal planar geometry. A similar effect was discussed excessively for the role of isovalent $Hg^{2+}$ and $Cd^{2+}$ in PbSe.[12, 17] We find that the Ag atoms are energetically more favorable by 16 meV/Ag in distorted off-center position than the in proper octahedral position. In other words, a lower energy is achieved when the Ag atom is shifted away from the regular site along the [110] direction by about 0.04 Å (Figure S9). This phenomenon can be attributed to the short Ag-Se average bond length of 2.701 Å in $AgSe_4$ tetrahedron of $Ag_2Se$ compound with orthorhombic structure. Therefore, when the Ag atom replaces Pb, we expect a locally distorted $AgSe_6$ octahedron and avoid the rock salt NaCl structure type. We refer to this behavior as discordant.[17-18] According to the energy profile calculation, the nearest neighbor averaged distance between Ag and Se is 2.925 Å, which is smaller than that of Ag in a regular Pb site of Ag-Se bond length 2.933 Å and even smaller than the Pb-Se bond length of 3.04 A. The off-centered Ag atoms not only reduce phonon velocity but also produce local strain with low frequency optical vibration modes, leading to reduced lattice thermal conductivity.

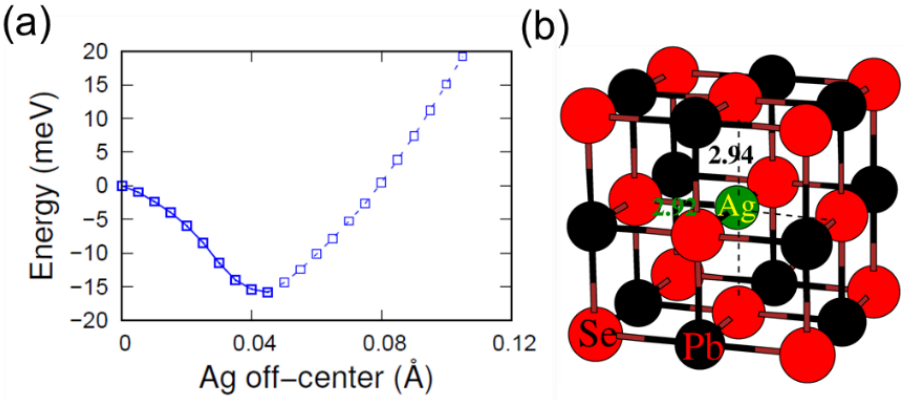


**Figure S9**. (a) The energy profile of Ag-doped PbSe as a function of coordinates from regular Ag substituted Pb of the octahedral site along [110] direction; and (b) illustration of the Ag off-center structure model with typical bond lengths of Ag–Se and Pb–Se. The normal bond length of Pb–Se is 3.10 Å and the average Ag-Se bond length is 2.93 Å for off-centered Ag in PbSe matrix.

# SUPPORTING INFORMATION

**Hall coefficients, carrier densities and mobility.** The measured Hall coefficients indicate p-type transport and yield carrier densities ($n$) in the low to mid $10^{19}$ $cm^{-3}$, Figure S10. The substitution of Sr and Ba for Pb in the rock salt lattice with 1% Ag doping typically increases the Hall coefficient, $R_H$, suggesting a decrease in hole carrier concentration, with the Ba having a slightly larger effect for a given mol%.

The Ag-doped samples feature a maximum in the Hall coefficient $T_H$ at around 550 K, which is far below the 1000 K of the valence band convergence temperature in pure PbSe,[19] Figure S11a and Table S1. In p-type PbTe- and PbSe-based compounds the occurance of $T_H$ as a maximum in the Hall coefficient signifies the convergence temperature of the two valence bands.[2a, 20] This $T_H$ observed in the present samples is the lowest temperature reported in PbSe-based material systems,[2a, 11, 17, 20] indicating the smallest $\Delta E_V$ value obtained.[20] There is no sign of a structural phase transition from the differential scanning calorimetry (DSC) curve (Figure S12b), so the peak must be electronic in nature. Similar to p-type PbTe we attribute such behavior to electronic energy band convergence,[13, 21] specifically between the valence bands in Ag-doped PbSe at around 560 K which is lower than the 700 K temperature occurring in Na-doped PbSe.[22] The lower temperature reflects the decreased energy difference $\Delta E_v$ in the alloyed materials. The aforementioned PYSA measurements independently point to the reduced energy band separation (smaller $\Delta E_v$) in the alloyed samples and the DFT calculations to be present below also predict a decreased $\Delta E_v$ in these systems.

As shown in Figure S11b, the 1% Ag-doped PbSe, 1.5% SrSe and 3% BaSe alloyed samples show the superior room temperature charge Hall carrier mobility, $\mu_H$, of ~280, ~230 and 257 $cm^2V^{-1}s^{-1}$ compared to previous p-type PbSe-based materials.[2a, 20] [23] [24] [12] Moreover, the mobility value of ~280 $cm^2V^{-1}s^{-1}$ for 1% Ag-doped PbSe is higher than that of the ~230 $cm^2V^{-1}s^{-1}$ for Na-doped PbSe standard sample with $n$ ~5.99 × $10^{19}$.[23]

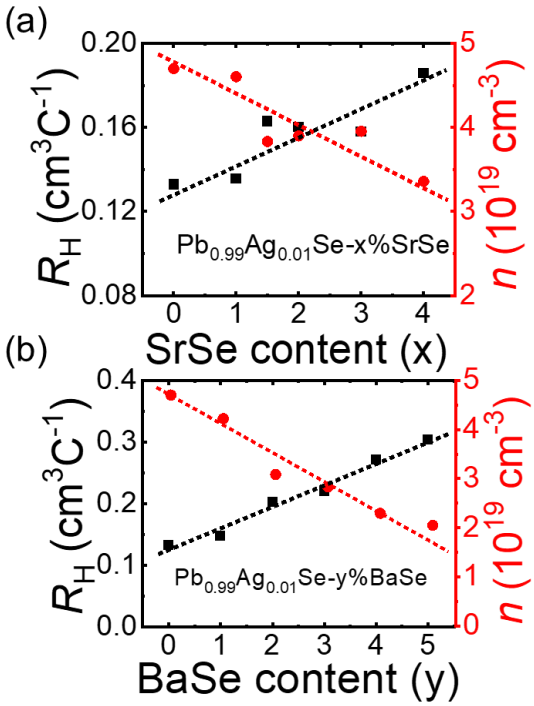


**Figure S10**. Hall coefficients, $R_H$, and charge carrier concentration, $n$, at 300 K for $Pb_{0.99}Ag_{0.01}Se$-x%SrSe (a) and $Pb_{0.99}Ag_{0.01}Se$-y%BaSe (b); The dashed lines are guides to the eye.

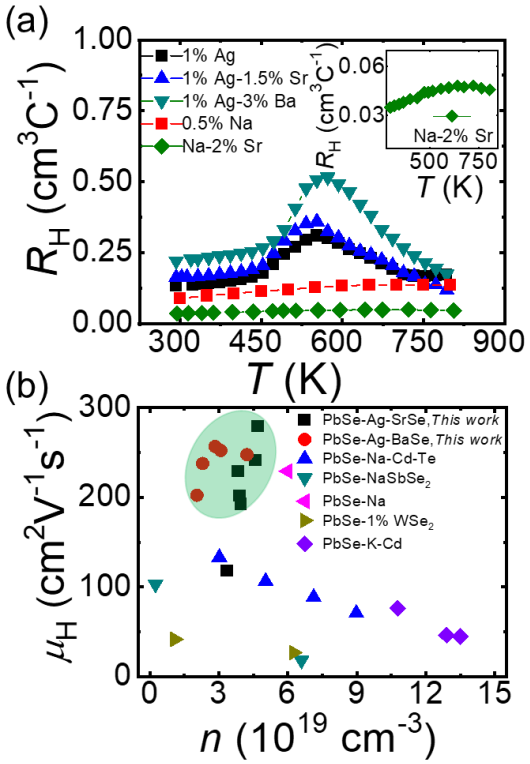


**Figure S11.** Temperature-dependent Hall coefficients $R_H$ for $Pb_{0.99}Ag_{0.01}Se$ (1% Ag), $Pb_{0.99}Ag_{0.01}Se$-1.5%SrSe (1% Ag-1.5% Sr), $Pb_{0.99}Ag_{0.01}Se$-3%BaSe (1% Ag-3% Ba), $Pb_{0.995}Na_{0.005}Se$ (0.5% Na)[22] and $Pb_{0.98}Na_{0.02}Se$-2%SrSe (Na-2% Sr)[11] samples. The inset shows an expanded view of $R_H$ for the $Pb_{0.98}Na_{0.02}Se$-2%SrSe (Na-2% Sr)[11] sample. (b) Comparison of carrier mobility, $\mu_H$ at room temperature in this work (PbSe-Ag-SrSe and PbSe-Ag-BaSe) with previous PbSe based samples: $Pb_{0.97-x}Na_xCd_{0.03}Se_{0.85}Te_{0.15}$ (PbSe-Na-Cd-Te),[20] PbSe–$NaSbSe_2$,[2a] PbSe-Na,[23] PbSe-1%$WSe_2$[24] and $Pb_{0.98}K_{0.02}Se$–x%CdSe (PbSe-K-Cd).[12]

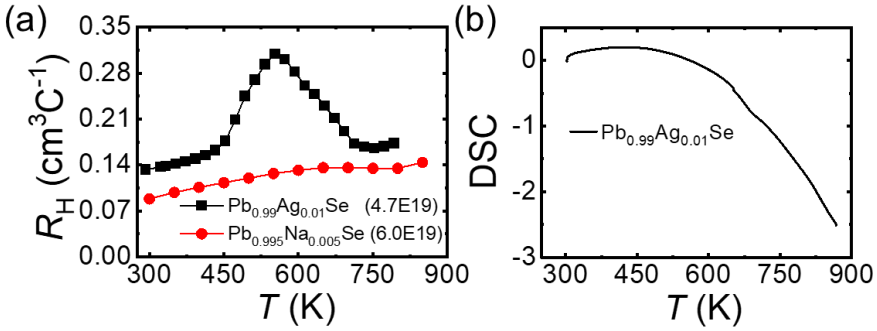


**Figure S12.** Temperature-dependent $R_H$ for $Pb_{0.99}Ag_{0.01}Se$ and $Pb_{0.995}Na_{0.005}Se$[22] with similar carrier concentration (a) and DSC curve of $Pb_{0.99}Ag_{0.01}Se$ sample.

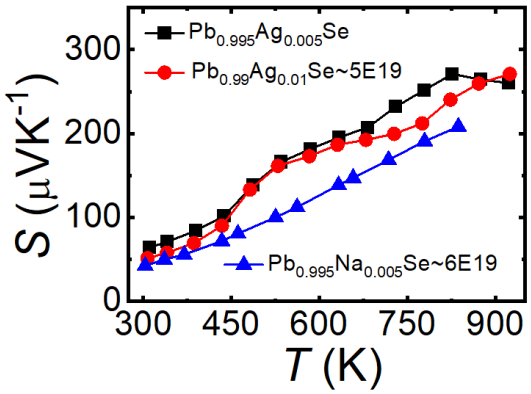


**Figure S13.** Temperature-dependent Seebeck coefficient of $Pb_{0.995}Ag_{0.005}Se$ and $Pb_{0.99}Ag_{0.01}Se$ ($n$ ~5 × $10^{19}$ $cm^{-3}$) with the $Pb_{0.995}Na_{0.005}Se$ ($n$ ~6 × $10^{19}$ $cm^{-3}$) data as a comparison.[22]

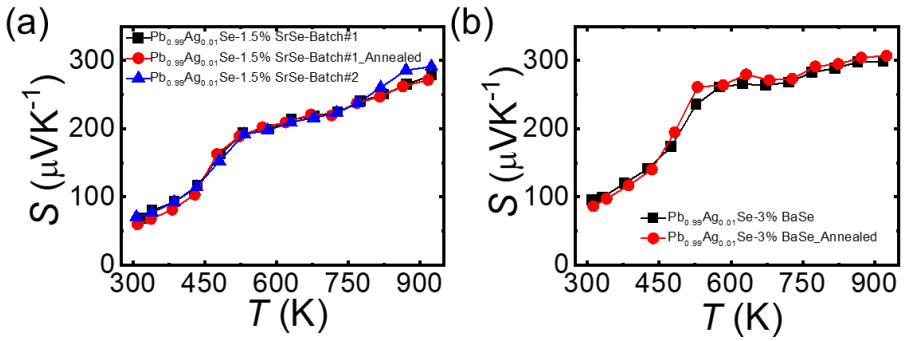


**Figure S14**. The Seebeck coefficient for $Pb_{0.99}Ag_{0.01}Se$-1.5%SrSe with different batches (a) and $Pb_{0.99}Ag_{0.01}Se$-3%BaSe (b) before and after 20 hours annealing at 873 K.

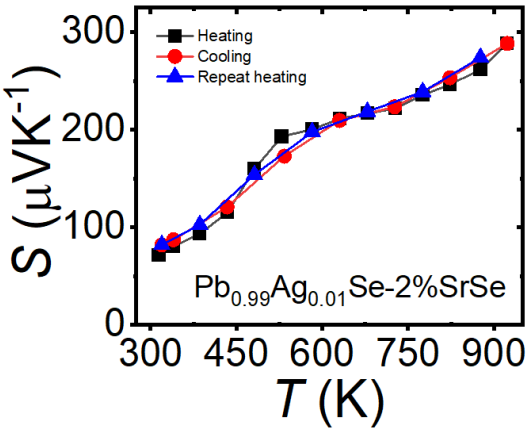


**Figure S15**. The Seebeck coefficient for $Pb_{0.99}Ag_{0.01}Se$-2%SrSe with the heating-cooling-repeat heating measurement procedure.

**Pisarenko plots.** The room temperature Seebeck coefficients as a function of carrier concentration, *n*, (the so-called Pisarenko relation) for all samples are plotted in Figures S16a and S16b. The solid curve represents the theoretically calculated value based on the single parabolic band (SPB) model for p-type PbSe with density-of-states (DOS) effective mass, *m**, of 0.28 $m_e$ ($m_e$ is the rest electron mass). The temperature-dependent Pisarenko relation for $Pb_{0.99}Ag_{0.01}Se$ (solid square), $Pb_{0.99}Ag_{0.01}Se$-1.5%SrSe (up-triangle) and $Pb_{0.99}Ag_{0.01}Se$-3%BaSe (down-triangle) samples with the *m** of 0.4 $m_e$ at 300 K (black), 573 K (dark yellow) and 773 K (red) are displayed in Figure S16c. The experimental results fit the theoretical curves nicely with *m** = ~0.4 $m_e$ at 300 K. Compared with the *m** of Na-doped PbSe (~0.28 $m_e$) and pure PbSe (~0.27 $m_e$), the Ag-doped and SrSe- or BaSe-alloyed PbSe samples have essentially 50% higher *m**. With the rising temperature, the *m** enlarges greatly as indicated by the position of the data points far above the theoretical curves, especially for 773 K (Figure S16c).

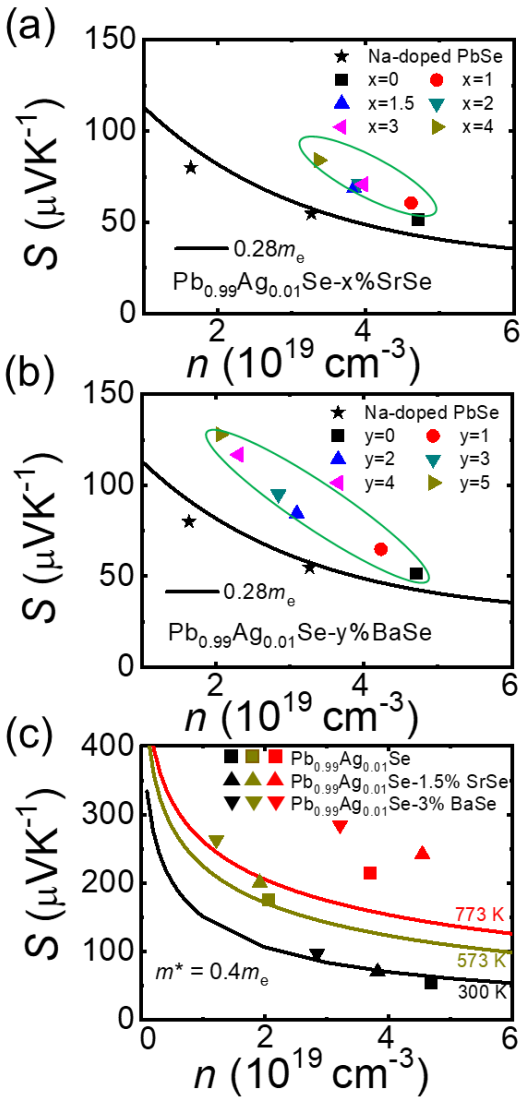


**Figure S16**. Seebeck coefficient as a function of Hall carrier concentration for $Pb_{0.99}Ag_{0.01}Se$-x%SrSe (a) and $Pb_{0.99}Ag_{0.01}Se$-y%BaSe (b) at 300 K. The solid curves are the theoretical Pisarenko plots for p-type PbSe with effective mass of electrons of 0.28 $m_e$; (c) Seebeck coefficient as a function of Hall carrier concentration with an effective mass of 0.4 $m_e$. The curves are the theoretical Pisarenko plots at 300 K (black), 573 K (dark yellow) and 773 K (red). The solid squares, up-triangles, and down-triangles represent $Pb_{0.99}Ag_{0.01}Se$, $Pb_{0.99}Ag_{0.01}Se$-1.5%SrSe and $Pb_{0.99}Ag_{0.01}Se$-3%BaSe, respectively.

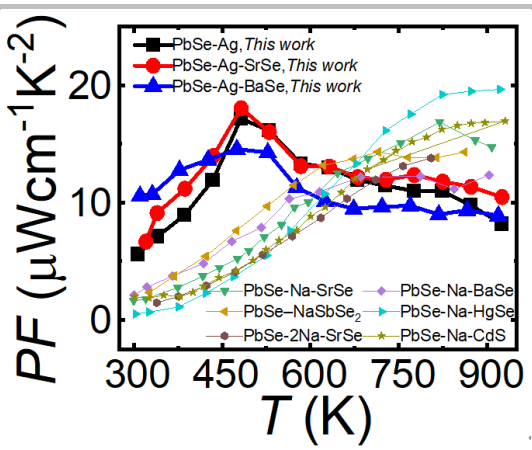


**Figure S17**. Comparison of power factor values for p-type PbSe-based materials in this study with previously explored $Pb_{0.99}Na_{0.01}Se$-2%SrSe (PbSe-Na-SrSe),[25] $Pb_{0.99}Na_{0.01}Se$-3%BaSe (PbSe-Na-BaSe),[25] $Na_{1.1}Pb_{10}Sb_{0.9}Se_{12}$ (PbSe–$NaSbSe_2$),[2a] $Pb_{0.98}Na_{0.02}Se$-2%HgSe (PbSe-Na-HgSe),[17] PbSe-2%Na-2%SrSe (PbSe-2Na-SrSe),[8] and PbSe-2%Na-3%CdS (PbSe-N a-CdS)[26] p-type PbSe thermoelectric materials.

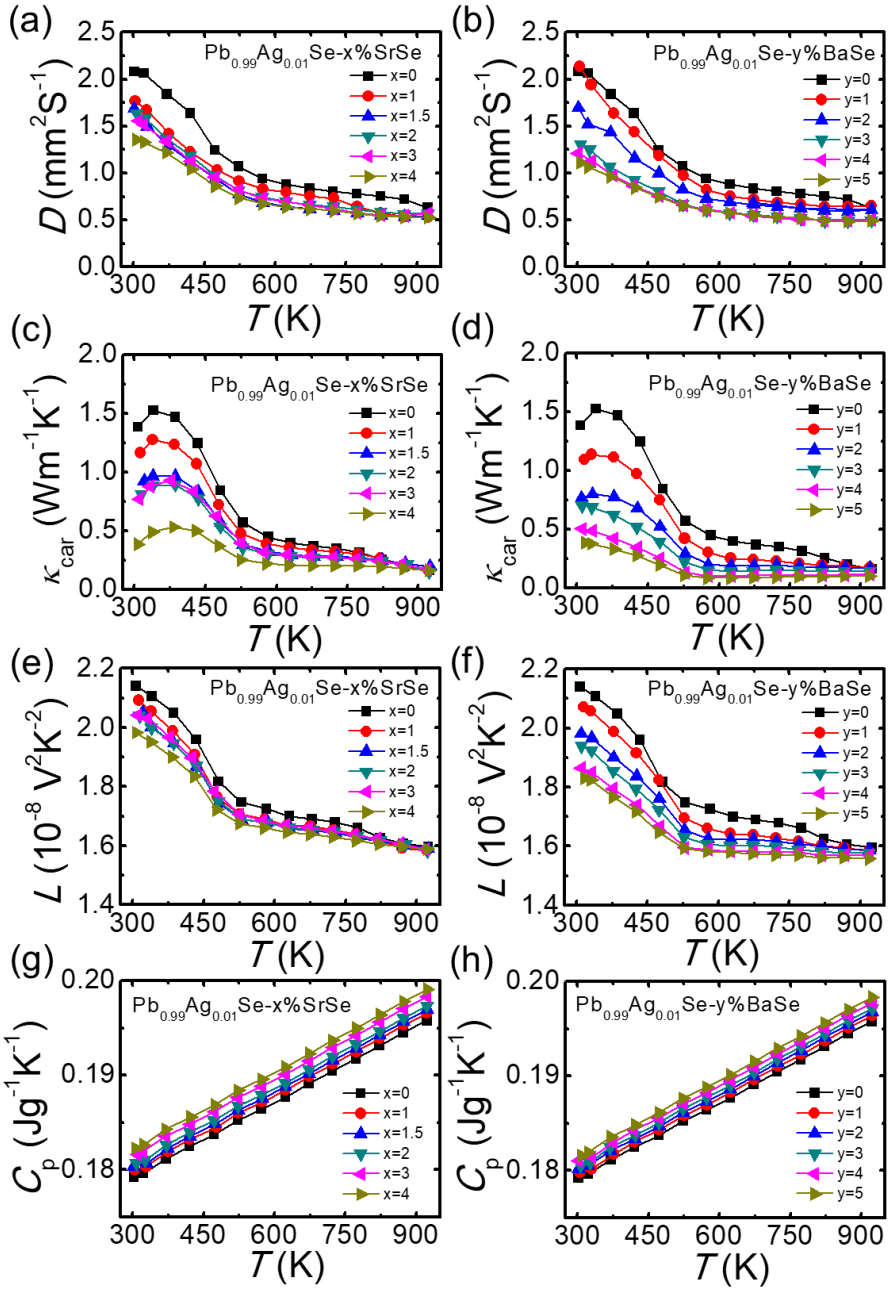


**Figure S18**. Thermoelectric properties as a function of temperature for $Pb_{0.99}Ag_{0.01}Se$-x%SrSe and $Pb_{0.99}Ag_{0.01}Se$-y%BaSe: thermal diffusivity, $D$, (a) and (b); electronic thermal conductivity, $\kappa_{car}$, (c) and (d); Lorenz numbers, $L$, (e) and (f); and heat capacity, $C_p$, (g) and (h).

# SUPPORTING INFORMATION

**Table S1.** Computational and experimental verification of the valance band convergence effect for this work and top performing p-type PbSe-based materials with Hall coefficient peaking temperature ($T_H$)

| | Calculation | Experiment | $T_H$ | Ref. |
|---|---|---|---|---|
| PbSe-Ag-Sr | DFT | Hall & PYSA | ~550 K | *This work* |
| PbSe–$NaSbSe_2$ | DFT | Hall & PYSA | ~610 K | [2a] |
| PbSe–Na-Hg | DFT | Hall | ~575 K | [17] |
| PbSe-Na-CdS | DFT | Hall | ~622 K | [26] |
| PbSe–K-Cd | DFT | PYSA | N | [12] |
| PbSe–Na-Cd-Te | DFT | Hall & PYSA | ~600 K | [20] |
| Pb1-xSrxSe-Na | KKR-CPA | Hall | ~703 K | [11] |
| $K_{0.02}Pb_{0.98}Te_{1-y}Se_y$ | Theoretical fittings | N | N | [27] |
| PbSe-Na-CdTe | DFT | N | N | [28] |

# SUPPORTING INFORMATION

**Table S2.** Room temperature mass densities for $Pb_{0.99}Ag_{0.01}Se$-x%SrSe and $Pb_{0.99}Ag_{0.01}Se$-y%BaSe samples.

| Composition | Measured Density, g/cm$^3$ | Theoretical Density, % |
|---|---|---|
| $Pb_{0.99}Ag_{0.01}Se$ | 8.11 | 98.5% |
| $Pb_{0.99}Ag_{0.01}Se$-1%SrSe | 8.03 | 98.0% |
| $Pb_{0.99}Ag_{0.01}Se$-1.5%SrSe | 7.95 | 97.2% |
| $Pb_{0.99}Ag_{0.01}Se$-2%SrSe | 7.95 | 97.4% |
| $Pb_{0.99}Ag_{0.01}Se$-3%SrSe | 7.91 | 97.3% |
| $Pb_{0.99}Ag_{0.01}Se$-4%SrSe | 7.98 | 98.6% |
| $Pb_{0.99}Ag_{0.01}Se$-1%BaSe | 8.06 | 98.2% |
| $Pb_{0.99}Ag_{0.01}Se$-2%BaSe | 8.00 | 97.7% |
| $Pb_{0.99}Ag_{0.01}Se$-3%BaSe | 7.97 | 97.6% |
| $Pb_{0.99}Ag_{0.01}Se$-4%BaSe | 7.87 | 96.6% |
| $Pb_{0.99}Ag_{0.01}Se$-5%BaSe | 7.95 | 97.8% |

## References


[1] T. J. McCarthy, S. P. Ngeyi, J. H. Liao, D. C. DeGroot, T. Hogan, C. R. Kannewurf, M. G. Kanatzidis, *Chem. Mater.* **1993**, *5*, 331-340.

[2] a) T. J. Slade, T. P. Bailey, J. A. Grovogui, X. Hua, X. Zhang, J. J. Kuo, I. Hadar, G. J. Snyder, C. Wolverton, V. P. Dravid, C. Uher, M. G. Kanatzidis, *Adv. Energy Mater.* **2019**, 1901377; b) I. D. Baikie, A. Grain, J. Sutherland, J. Law, *physica status solidi c* **2015**, *12*, 259-262.

[3] K. A. Borup, J. de Boor, H. Wang, F. Drymiotis, F. Gascoin, X. Shi, L. Chen, M. I. Fedorov, E. Müller, B. B. Iversen, G. J. Snyder, *Energy Environ. Sci.* **2015**, *8*, 423-435.

[4] R. Blachnik, R. Igel, in *Zeitschrift für Naturforschung B, Vol. 29*, **1974**, p. 625.

[5] Z.-Z. Luo, S. Hao, X. Zhang, X. Hua, S. Cai, G. Tan, T. P. Bailey, R. Ma, C. Uher, C. Wolverton, V. P. Dravid, Q. Yan, M. G. Kanatzidis, *Energy Environ. Sci.* **2018**, *11*, 3220-3230.

[6] J. P. Perdew, K. Burke, M. Ernzerhof, *Phys. Rev. Lett.* **1997**, *78*, 1396-1396.

[7] G. Kresse, J. Furthmüller, *Phys. Rev. B* **1996**, *54*, 11169-11186.

[8] L. Zeng, J. Zhang, L. You, H. Zheng, Y. Liu, L. Ouyang, P. Huang, J. Xing, J. Luo, *J. Alloys Compd.* **2016**, *687*, 765-772.

[9] X. Zhang, L. Liang, J. Zhang, Q. Su, *Mater. Lett.* **2005**, *59*, 749-753.

[10] V. V. Sobolev, D. A. Merzlyakov, V. V. Sobolev, *J. Appl. Spectrosc.* **2017**, *84*, 255-260.

[11] H. Wang, Z. M. Gibbs, Y. Takagiwa, G. J. Snyder, *Energy Environ. Sci.* **2014**, *7*, 804-811.

[12] S. Cai, S. Hao, Z.-Z. Luo, X. Li, I. Hadar, T. P. Bailey, X. Hu, C. Uher, Y.-Y. Hu, C. Wolverton, V. P. Dravid, M. G. Kanatzidis, *Energy Environ. Sci.* **2020**, *13*, 200-211.

[13] T. C. Chasapis, Y. Lee, E. Hatzikraniotis, K. M. Paraskevopoulos, H. Chi, C. Uher, M. G. Kanatzidis, *Phys. Rev. B* **2015**, *91*, 085207.

[14] H. Billetter, U. Ruschewitz, *Z. Anorg. Allg. Chem.* **2008**, *634*, 241-246.

[15] M. G. Kanatzidis, S.-P. Huang, *Angew. Chem. Int. Ed.* **1989**, *28*, 1513-1514.

[16] E. Gaudin, F. Boucher, M. Evain, *J. Solid State Chem.* **2001**, *160*, 212-221.

[17] J. M. Hodges, S. Hao, J. A. Grovogui, X. Zhang, T. P. Bailey, X. Li, Z. Gan, Y. Y. Hu, C. Uher, V. P. Dravid, C. Wolverton, M. G. Kanatzidis, *J. Am. Chem. Soc.* **2018**, *140*, 18115-18123.

[18] Z. Z. Luo, S. Cai, S. Hao, T. P. Bailey, X. Su, I. Spanopoulos, I. Hadar, G. Tan, Y. Luo, J. Xu, C. Uher, C. Wolverton, V. P. Dravid, Q. Yan, M. G. Kanatzidis, *J. Am. Chem. Soc.* **2019**, *141*, 16169-16177.

[19] Z. M. Gibbs, H. Kim, H. Wang, R. L. White, F. Drymiotis, M. Kaviany, G. J. Snyder, *Appl. Phys. Lett.* **2013**, *103*, 262109.

[20] G. Tan, S. Hao, S. Cai, T. P. Bailey, Z. Luo, I. Hadar, C. Uher, V. P. Dravid, C. Wolverton, M. G. Kanatzidis, *J. Am. Chem. Soc.* **2019**, *141*, 4480-4486.

[21] R. S. Allgaier, B. B. H. Jr., *J. Appl. Phys.* **1966**, *37*, 302-309.

[22] H. Wang, Y. Pei, A. D. LaLonde, G. J. Snyder, *Adv. Mater.* **2011**, *23*, 1366-1370.
[23] Y. Lee, S.-H. Lo, J. Androulakis, C.-I. Wu, L.-D. Zhao, D.-Y. Chung, T. P. Hogan, V. P. Dravid, M. G. Kanatzidis, *J. Am. Chem. Soc.* **2013**, *135*, 5152-5160.
[24] Q. Lin, S. Tepfer, C. Heideman, C. Mortensen, N. Nguyen, P. Zschack, M. Beekman, D. C. Johnson, *J. Mater. Res.* **2011**, *26*, 1866-1871.
[25] Y. Lee, S. H. Lo, J. Androulakis, C. I. Wu, L. D. Zhao, D. Y. Chung, T. P. Hogan, V. P. Dravid, M. G. Kanatzidis, *J. Am. Chem. Soc.* **2013**, *135*, 5152-5160.
[26] L.-D. Zhao, S. Hao, S.-H. Lo, C.-I. Wu, X. Zhou, Y. Lee, H. Li, K. Biswas, T. P. Hogan, C. Uher, C. Wolverton, V. P. Dravid, M. G. Kanatzidis, *J. Am. Chem. Soc.* **2013**, *135*, 7364-7370.
[27] Q. Zhang, F. Cao, W. Liu, K. Lukas, B. Yu, S. Chen, C. Opeil, D. Broido, G. Chen, Z. Ren, *J. Am. Chem. Soc.* **2012**, *134*, 10031-10038.
[28] Z. Huang, D. Wang, C. Li, J. Wang, G. Wang, L.-D. Zhao, *J. Mater. Chem. A* **2020**, *8*, 4931-4937.

## Author Contributions

Z.Z.L, Q.Y., and M.G.K. prepared the samples, designed, carried out thermoelectric experiments, and analysed the electrical and thermal transport data. S.C. and V.P.D. carried out the TEM experiment and analysed the TEM data. S.H. and C.W. carried out the DFT calculations. T. P. B., and C. U. carried out the Hall measurements. Z.Z.L, Q.Y., and M.G.K. interpreted all results and wrote and edited the manuscript. All authors have reviewed, discussed and approved the results and conclusions of this article.